

Space-Projected Thermal Conductivity

A. Gautam^{a,1}, Y. G. Lee^{a,2}, C. Ugwumadu^b, K. Nepal^{a,1}, S. Nakhmanson^c, D. A. Drabold^{a,1}

^aDepartment of Physics and Astronomy, Ohio University, Athens, 45701, OH, USA

^bPhysics of Condensed Matter and Complex Systems (T-4) Group, Los Alamos National Laboratory, Los Alamos, 87545, NM, USA

^cDepartment of Physics, Department of Materials Science & Engineering, Institute of Materials Science, University of Connecticut, Storrs, 06269, CT, USA

Abstract

With the rapid advancement of high-power computing and electronic technologies, understanding thermal conductivity in materials has become increasingly important. This study presents a novel method called the *Space-Projected Thermal Conductivity* (SPTC) that can predict thermal activity at the atomic scale, leveraging the Green-Kubo thermal transport equations. We demonstrate the effectiveness of this approach on crystalline and amorphous carbon-based structures, paracrystalline and amorphous silicon, and grain boundaries in silicon-germanium alloys. The results highlight the potential of our method to provide new insights into the thermal behavior of materials, offering a promising avenue for materials design and performance optimization.

1. Introduction

The investigation of thermal transport properties in materials is a rapidly evolving field of research [1, 2, 3, 4]. A key challenge lies in identifying and characterizing thermally active sites, which is crucial for understanding and predicting thermal transport behavior. While spatially resolved models for electronic transport have been successfully developed and applied to a broad range of materials [5, 6, 7, 8, 9, 10, 11], achieving a similarly comprehensive representation of thermally active sites remains an area of intense and ongoing research.

In this study, we present the *Space-Projected Thermal Conductivity* (SPTC) method, which offers an intuitive framework for identifying thermally active sites within materials in real space. We adopt the Allen and Feldman approach [12] to derive an expression for thermal conductivity using the Green-Kubo formalism for thermal transport [13]. The SPTC method is applied to a range of crystalline, defective, and amorphous materials, including carbon and silicon allotropes. Additionally, we investigate the thermal properties of interfaces and grain boundaries in paracrystalline silicon and silicon-germanium alloy systems. It is important to note that this method accounts solely for phonon contributions to heat transport, excluding electronic effects.

2. Theory

The theory of Allen and Feldman [12], tersely recounted here, is a method for computing and understanding thermal transport in materials in the harmonic approximation. Their

starting point is Kubo's expression for the thermal conductivity tensor, $\kappa_{\mu\nu}$:

$$\kappa_{\mu\nu}(\omega) = \frac{V}{T} \int_0^{1/k_B T} d\tau \int_0^\infty dt e^{j(\omega+i\eta)t} \langle S_\mu(-i\hbar\tau) S_\nu(t) \rangle. \quad (1)$$

Here, V and T are the volume and the temperature of the system, μ and ν are the Cartesian components of the heat current operator \mathbf{S} , and $\langle \dots \rangle$ is the current-current autocorrelation function. Hardy's form for \mathbf{S} is (with atoms indexed by Latin indices and directions by Greek indices α, β):

$$\mathbf{S} = -\frac{1}{2V} \sum_{i,j} \sum_{\alpha,\beta} (\mathbf{R}_i - \mathbf{R}_j) \frac{p_{i\alpha}}{m_i} \frac{\partial^2 E}{\partial u_i^\alpha \partial u_j^\beta} u_j^\beta. \quad (2)$$

where, \mathbf{R}_i in the position of i^{th} atom in the unit cell. Invoking the usual harmonic approximation (HA), the classical Hamiltonian is:

$$\mathcal{H} = \sum_i \frac{p_i^2}{2m_i} + \frac{1}{2} \sum_{i,j} \frac{\partial^2 E}{\partial u_i \partial u_j} u_i u_j, \quad (3)$$

where p_i and u_i are the momenta and small displacements. The potential energy, E , is given as:

$$E = \frac{1}{2} \sum_{\gamma,\gamma'} \sum_{i,j} \sum_{\alpha,\beta} \phi_{i,j}^{\alpha\beta}(\gamma,\gamma') u_{\gamma i}^\alpha u_{\gamma' j}^\beta \quad (4a)$$

$$\phi_{i,j}^{\alpha\beta}(\gamma,\gamma') = \frac{\partial^2 E}{\partial u_{\gamma i}^\alpha \partial u_{\gamma' j}^\beta}. \quad (4b)$$

Here, $\phi_{i,j}^{\alpha\beta}(\gamma,\gamma')$ is the force constant matrix, and γ and γ' represent the cells in the periodic system. From the classical equations of motion:

Email address: drabold@ohio.edu (D. A. Drabold)

¹Also at Nanoscale & Quantum Phenomena Institute, Ohio University

²Also at Institute of Nuclear and Particle Physics, Ohio University

$$\omega^2 u_i^{\alpha, \mathbf{k}} = \sum_{\beta j} D_{ij}^{\alpha\beta}(\mathbf{k}) u_j^{\beta, \mathbf{k}}, \quad (5a)$$

$$D_{ij}^{\alpha\beta}(\mathbf{k}) = \sum_{\gamma} \frac{1}{\sqrt{m_i m_j}} \phi_{i,j}^{\alpha\beta}(0, \gamma) e^{i\mathbf{k} \cdot (\mathbf{R}_{j,\gamma} - \mathbf{R}_{i,0})} \quad (5b)$$

$D_{ij}^{\alpha\beta}(\mathbf{k})$ is the Dynamical Matrix (DM), the Fourier transform of the force constant matrix. $\mathbf{R}_{j,\gamma}$ is the position of j^{th} atom in the γ^{th} cell. \mathbf{k} is a wave vector that may be chosen at the center or corner of the Brillouin zone. For N cells in a system with l atoms per cell, labeled by $x = 1, 2, \dots, l$; the \mathbf{S} operator from Equation 2 is transformed to:

$$\mathbf{S} = \sum_{m,n} \mathbf{S}_{mn} \hat{a}_m^\dagger \hat{a}_n \quad (6a)$$

$$\mathbf{S}_{mn} = \frac{\hbar}{2V} \mathbf{v}_{mn}^{\mathbf{k}} (\omega_m^{\mathbf{k}} + \omega_n^{\mathbf{k}}) \quad (6b)$$

Here, m, n are the indices of the phonon modes; \hat{a}_m^\dagger and \hat{a}_n are the creation and annihilation operators of a phonon mode respectively; $\mathbf{v}_{mn}^{\mathbf{k}}$ is the group velocity vector of mode m when $m = n$; $\omega_m^{\mathbf{k}}$ is the vibrational frequency of the mode m . Upon applying the harmonic approximation results on Equation 1, a general expression for the real part of TC is obtained [12]:

$$\kappa_{\alpha\beta}(\omega) = \frac{\pi V}{T} \sum_{m,n} \left[\frac{\langle f_m \rangle - \langle f_n \rangle}{\hbar(\omega_m - \omega_n)} \right] (S^\alpha)_{mn} (S^\beta)_{nm} \delta(\omega_m^{\mathbf{k}} - \omega_n^{\mathbf{k}} - \omega) \quad (7)$$

where, f_m is the equilibrium occupation of the m^{th} mode (i.e., the Bose-Einstein phonon distribution); $(S^\alpha)_{mn}$ is the α^{th} component of S_{mn} . When $\omega \rightarrow 0$, due to the presence of the δ function, the term $\frac{\langle f_m \rangle - \langle f_n \rangle}{\hbar(\omega_m - \omega_n)}$ in Equation 7 simplifies to $-\partial \langle f_m \rangle / \partial \omega_m$. With these considerations, and using Equations 6, Allen and Feldman's formulation for TC is expressed as:

$$\begin{aligned} \kappa = & \frac{1}{V} \sum_{m,n \neq m} \frac{\pi V^2}{3\hbar^2 \omega_m^2} \frac{\hbar \omega_m^2}{T} \left[\frac{-\partial \langle f_m \rangle}{\partial \omega_m} \right] \left(\frac{\hbar}{2V} \right)^2 (\omega_m^{\mathbf{k}} + \omega_n^{\mathbf{k}})^2 \frac{\delta(\omega_m^{\mathbf{k}} - \omega_n^{\mathbf{k}})}{4\omega_m^{\mathbf{k}} \omega_n^{\mathbf{k}}} \\ & \sum_{\eta} \sum_{\alpha\beta} \sum_{\gamma, x, x'} e_{x,\mathbf{k}}^{\alpha, m} e_{x',\mathbf{k}}^{\beta, n} \frac{1}{\sqrt{m_x m_{x'}}} \phi_{x,x'}^{\alpha\beta}(0, \gamma) (R_\gamma^\eta + R_{xx'}^\eta) \\ & \sum_{\alpha'\beta'} \sum_{\gamma', a, b} e_{a,\mathbf{k}}^{\alpha', m} e_{b,\mathbf{k}}^{\beta', n} \frac{1}{\sqrt{m_a m_b}} \phi_{a,b}^{\alpha'\beta'}(0, \gamma') (R_{\gamma'}^\eta + R_{ab}^\eta) \quad (8) \end{aligned}$$

where, R_γ^η is the η component of position vector for cell γ ; $R_{xx'}^\eta$ is the η component of displacement between atoms x and x' ; $e_{x,\mathbf{k}}^{\alpha, m}$ is the polarization of the vibrational mode m at atom x along α direction. The thermal conductivity in Equation 8, is taken as an average of the Cartesian components of the conductivity tensor. In the case of $\mathbf{k} = \mathbf{0}$, Equation 8 is reorganized

as:

$$\begin{aligned} \kappa = & \frac{1}{V} \sum_{\eta} \sum_{\gamma, x, x'} \frac{1}{\sqrt{m_x m_{x'}}} (R_\gamma^\eta + R_{xx'}^\eta) \sum_{m, n \neq m} \delta(\omega_m^{\mathbf{0}} - \omega_n^{\mathbf{0}}) \\ & \frac{\pi V^2}{3\hbar^2 \omega_m^2} \left(\frac{\hbar}{2V} \right)^2 (\omega_m^{\mathbf{0}} + \omega_n^{\mathbf{0}})^2 \frac{1}{4\omega_m^{\mathbf{0}} \omega_n^{\mathbf{0}}} \frac{\hbar \omega_m^2}{T} \\ & \left(\frac{\hbar}{k_B T} \frac{e^{\frac{\hbar \omega_m}{k_B T}}}{\left(e^{\frac{\hbar \omega_m}{k_B T}} - 1 \right)^2} \right) \sum_{\alpha\beta} \phi_{x,x'}^{\alpha\beta}(0, \gamma) e_{x,\mathbf{0}}^{\alpha, m} e_{x',\mathbf{0}}^{\beta, n} \\ & \sum_{\gamma', a, b} \sum_{\alpha'\beta'} \frac{1}{\sqrt{m_a m_b}} \phi_{a,b}^{\alpha'\beta'}(0, \gamma') e_{a,\mathbf{0}}^{\alpha', m} e_{b,\mathbf{0}}^{\beta', n} (R_{\gamma'}^\eta + R_{ab}^\eta) \quad (9) \end{aligned}$$

2.1. The Space-Projected Thermal Conductivity Formalism

To this point, we have only recounted the work of Allen and Feldman. In this section, we seek to extract spatial information about thermal conduction within the Allen and Feldman picture. As we have shown for the electrical conductivity [5], simple rearrangements of expressions for the conductivity provide spatial information about conduction activity. That is, any Kubo formula may be rearranged such that the target conductivity is a double sum over spatial points (atomic sites in this case) x . We show that an informative expression for a spatially-resolved TC emerges as a result, providing the most obvious form for it in this paper. Other forms are possible, and we are exploring general considerations for an optimal form for SPTC.

Rearranging summation order in Equation 8, we can obtain an expression for κ as a (double) sum over terms depending on atomic positions x and x' :

$$\kappa = \sum_{x, x'} \Xi(x, x'), \quad (10)$$

where

$$\begin{aligned} \Xi(x, x') = & \frac{\pi \hbar^2}{48 k_B T^2 V} \frac{1}{\sqrt{m_x m_{x'}}} \sum_{\eta, \gamma} (R_\gamma^\eta + R_{xx'}^\eta) \sum_{m, n \neq m} \delta(\omega_m^{\mathbf{0}} - \omega_n^{\mathbf{0}}) \\ & \frac{(\omega_m^{\mathbf{0}} + \omega_n^{\mathbf{0}})^2}{\omega_m^{\mathbf{0}} \omega_n^{\mathbf{0}}} \left(\frac{e^{\frac{\hbar \omega_m}{k_B T}}}{\left(e^{\frac{\hbar \omega_m}{k_B T}} - 1 \right)^2} \right) \sum_{\alpha\beta} \phi_{x,x'}^{\alpha\beta}(0, \gamma) e_{x,\mathbf{0}}^{\alpha, m} e_{x',\mathbf{0}}^{\beta, n} \\ & \sum_{\gamma' a b} \sum_{\alpha'\beta'} \frac{1}{\sqrt{m_a m_b}} \phi_{a,b}^{\alpha'\beta'}(0, \gamma') e_{a,\mathbf{0}}^{\alpha', m} e_{b,\mathbf{0}}^{\beta', n} (R_{\gamma'}^\eta + R_{ab}^\eta). \quad (11) \end{aligned}$$

For $\omega = 0$, Ξ is a Hermitian matrix, i.e., $\Xi(x, x') = \Xi(x', x)$. Equation 10 suggests a way to decompose the total TC into contributions depending on atomic position x by conduction a summation of $\Xi(x, x')$ over all positions x' :

$$\zeta(x) = \sum_{x'} \Xi(x, x'). \quad (12)$$

Here, $\zeta(x)$ can be named the space-projected thermal conductivity (SPTC), as it represents the contribution of atom at site x to the total TC of the system. Summing $\zeta(x)$ over atom index x recovers the total TC κ :

$$\kappa = \sum_x \zeta(x). \quad (13)$$

3. Illustration of the Method

As a proof of concept, we conducted SPTC analysis on a range of different material systems, primarily carbon, silicon, and silicon-germanium structures. These systems included crystalline graphene, with both single and double vacancy defects, as well as amorphous graphene, characterized by ring disorder. Additionally, we applied SPTC analysis to diamond-crystalline silicon, paracrystalline silicon, and silicon-germanium alloy systems, with a focus on grain boundaries and mass defects.

Molecular dynamics (MD) simulations were conducted using Large-scale Atomic/Molecular Massively Parallel Simulator (LAMMPS) [14]. Within LAMMPS, the Machine Learning Gaussian approximation potential (ML-GAP) for carbon [15] and silicon [16] were employed for the carbon and pure silicon simulations. The Tersoff potential was used for the silicon-germanium structure [17].

Periodic boundary conditions were applied for all the simulations. The conjugate gradient algorithm was used for energy minimization (and structural optimization) with an energy convergence threshold of 10^{-10} eV. For the DM calculations, the atoms were displaced by 0.05 \AA in x -, y -, and z - directions, and the SPTC calculations were performed using Equation 12. The subsequent sections elaborate on the specific simulation protocols for the materials studied.

3.1. Carbon Structures

For the SPTC analysis of crystalline carbon systems, a structural model of crystalline graphene with surface dimensions of $29.4 \times 34.03 \text{ \AA}$ was utilized, as illustrated in Figure 1(a). To investigate the influence of vacancy defects on TC, we created models for (i) Stone-Wales defect [18] with pentagon-octagon-pentagon rings [henceforth referred to as SW-585] and (ii) a single-vacancy defect. The SW-585 model was constructed by removing two atoms from the graphene sheet and performing a structural relaxation. Both vacancy models are presented in Figure 1(b) and (c), respectively.

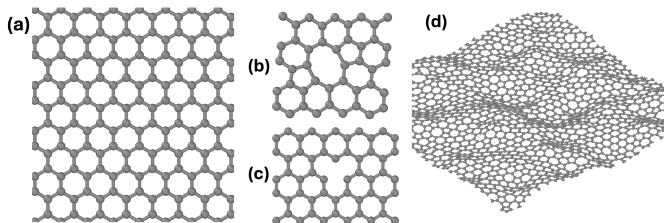


Figure 1: Representations of the carbon-based models: (a) crystalline graphene, (b) 585 Stone-Wales defect, (c) single vacancy defect, and (d) the undulating sp^2 structure of amorphous graphene.

The initial configuration of the 2000-atom amorphous graphene model (aGr₂₀₀₀) was generated by randomly distributing atoms within a cuboid measuring $72.30 \text{ \AA} \times 72.30 \text{ \AA} \times 4 \text{ \AA}$. The simulation followed the methodology for amorphous graphite outlined in References [19] and [20], with a modification during the heating process. The system was simulated in the canonical ensemble (NVT), controlled by a Nosé-Hoover

thermostat [21, 22, 23] at 2700 K. Zero force was applied in the z direction, restricting atomic movement to the XY plane. Afterward, the z dimension was extended by 3 \AA (on both sides), and the structure was annealed at 300 K for 50 ps before being relaxed, resulting in the undulating structure shown in Figure 1(d). We note that the amorphous graphene constructed in this study is highly defective but serves its purpose in revealing the effects of defects on thermal conduction pathways in disordered graphene. Less-defective amorphous graphene can be obtained using the methods described in References [24] and [25].

3.2. Silicon Single-Vacancy Defect

A diamond-structure Si unit cell was sourced from the Materials Project [26], and a 1000-atom, $5 \times 5 \times 5$ supercell model was constructed from it and used as the base for creating different Si structures. The original cubic supercell, with length of 27.21 \AA and density (ρ) of 2.33 g/cm^3 , was relaxed, exhibiting no significant change in its conformation. A single-vacancy defect, shown in Figure 2(a), was created by removing an atom from the crystalline Si lattice, followed by another energy/structural relaxation. For the analysis of the temperature and frequency dependence of TC in amorphous silicon (aSi), a tetrahedral Si model with 512 atoms ($\rho = 2.34 \text{ g/cm}^3$), obtained from Reference [27], was utilized.

3.3. Twin Grain Boundary in Silicon

A silicon grain boundary (GB) model, denoted as $\Sigma 3(112)/[1\bar{1}0]$, was obtained from Reference [28]. The cell dimensions are $9.46 \times 15.45 \times 100.60 \text{ \AA}^3$, with a separation of approximately 50.30 \AA between the two GB planes, as shown in Figure 2(b). The twin GB exhibits a misorientation characterized by a 60° rotation around the $[1\bar{1}0]$ axis, with one of the grains aligned along the (112) plane.

3.4. Alloy-Chemical Disorder ($Si_{1-x}Ge_x$ Structure)

To construct a $Si_{1-x}Ge_x$ structures, for $x = 0.25, 0.5$, and 0.75 , the silicon atoms in the diamond Si supercell discussed in Section 3.2 were randomly replaced with germanium atoms followed by conjugate gradient relaxation. Figure 2(c) shows a representation of the resulting structure. The $Si_{0.75}Ge_{0.25}$ composition was selected to investigate the effects of mass disorder on the thermal transport behavior.

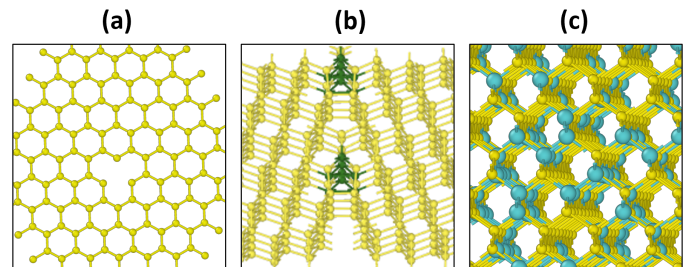


Figure 2: Representations of the silicon models (yellow spheres): (a) single-vacancy defect in diamond Si, (b) $\Sigma 3(112)/[1\bar{1}0]$ twin grain boundary, with five-fold coordinated Si atoms at the boundary shown as dark green spheres, and (c) silicon-germanium structure, where germanium atoms (cyan spheres) are randomly substituted for Si atoms in the diamond Si lattice.

4. Results and Discussion

4.1. Carbon Structures

Single-vacancy defects. The SPTC for three-fold coordinated hexagonal rings in crystalline graphene are uniformly distributed. However, introducing a single-atom vacancy in an otherwise crystalline graphene structure significantly reduces the TC of nearby atoms. The values for the two-fold coordinated carbon atoms near the vacancy is approximately 27% of that for the three-fold coordinated atoms in the bulk region.

As shown in Figure 3(a), the atoms adjacent to the vacancy (highlighted in blue) exhibit the lowest SPTC. An incremental, radially isotropic increase in normalized SPTC is observed moving outward from the defect center. To quantify anisotropy, the SPTC along two angular directions — 0° and 30° , marked by the red and green lines in Figure 3(a) — is shown in Figure 3(b). The variation in SPTC with distance follows a similar trend along both directions.

SW-585 defects. In the defective SW-585 configuration shown in Figure 3(c), the atoms in the five- and eight-membered rings are the lowest thermal conduction active sites, with the normalized SPTC reduced by approximately 60% compared to the bulk maximum. The SPTC gradually increases in all directions moving away from the defective region. The changes along two angular directions, 90° and 30° , represented by red and green lines in Figure 3(c), are illustrated in Figure 3(d). The

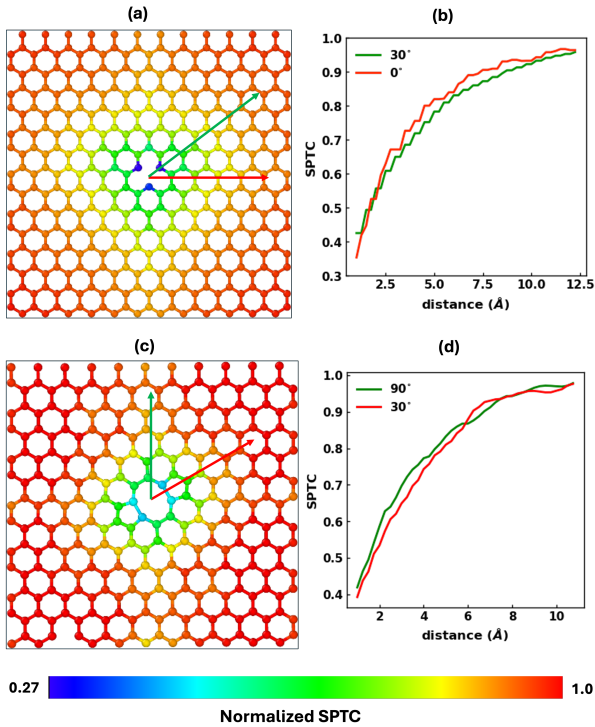


Figure 3: (a) Plot of the normalized SPTC results for a single vacancy in crystalline graphene. The incremental changes in SPTC values, originating from the defect center and radiating outward are plotted in (b). Likewise, the SPTC and their incremental changes from the defect center in the SW-585 crystalline graphene configuration are depicted in (c) and (d), respectively.

plot shows isotropic increment in SPTC, returning to the maximum (bulk) values at around 10 Å away from the defect center.

Amorphous graphene. In the aGr₂₀₀₀ model shown in Figure 4[i], atoms with only two neighbors exhibit SPTC values up to 74% of those of three-coordinated atoms. However, the SPTC for the three-coordinated carbon atoms vary depending on their local ring connectivity: atoms in non-hexagonal rings are less thermally active than those in hexagonal rings, similar to what is observed in crystalline graphene. To confirm this, a 60-atom amorphous graphene model (aGr₆₀) was created. Its SPTC analysis, shown in Figure 4[ii], also indicates higher values for hexagonal rings compared to non-hexagonal ones. The ring distribution for both amorphous graphene models is illustrated in Figure 4[iii].

We note a similarity between thermally and electronically conductive regions. References [19] and [20], which report the electronic transport properties of amorphous graphite, report that in the amorphous graphene layers, the hexagonal carbon rings favor electron flow, while connections between pentagonal and heptagonal rings impede it. Similar observation was made for ring disorder in amorphous carbon nanotubes [29].

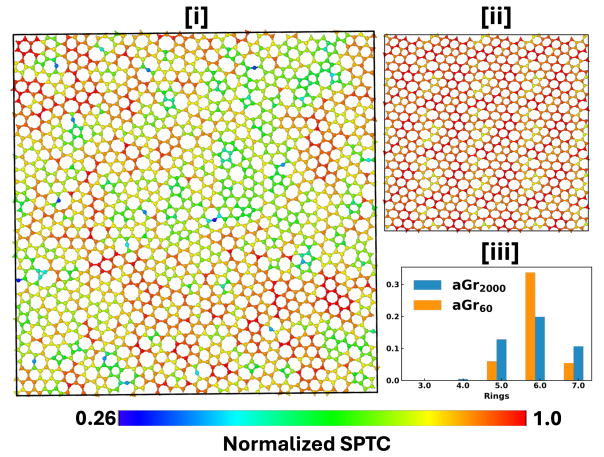


Figure 4: Normalized SPTC results for amorphous graphene with [i] 2000 atoms (aGr₂₀₀₀) and [ii] 60 atoms (aGr₆₀). The ring distribution for the aGr₂₀₀₀ and aGr₆₀ models is shown in [iii].

4.2. Silicon Structures

To test our implementation of Allen and Feldman formulation for the thermal conductivity [12], we compared the temperature and frequency dependence of TC in amorphous silicon produced by our implementation with the results of Feldman *et al.* [30], as shown in Figure 5(a) and (b). The TC temperature dependence obtained here is consistent with that in Reference [30], while the peak in the frequency dependence curve (the gray dashed line at 0.24 meV) matches the position they reported at 175 K. Note that the consistency is strong despite the use of a different interatomic potential and model in our work.

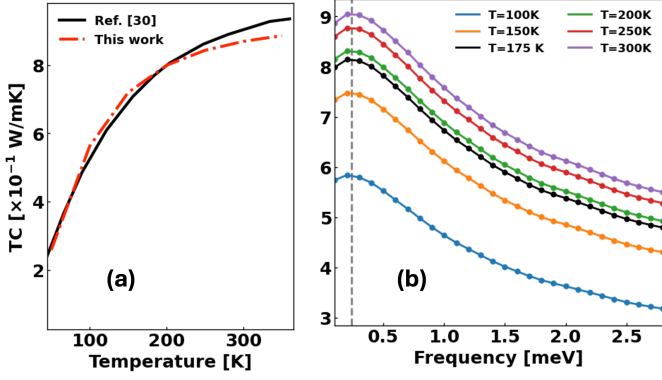


Figure 5: (a) Temperature dependence of TC for amorphous silicon, with results from this study compared to those of Feldman and coworkers [30]. (b) Frequency dependence of TC at various temperatures, with the dashed gray line marking the peak at 175 K. This peak aligns with the corresponding plot at the same temperature in Reference [30].

Diamond silicon and single-vacancy defect. In defect-free diamond-silicon structure, all atoms contribute equally to the total TC of the system. On the other hand, local TC on atomic sites in the vicinity of the single-vacancy defect is reduced. Such under-coordinated silicon atoms with dangling bonds exhibit $\approx 70\%$ reduction in SPTC, as compared to the bulk-crystal value. The SPTC evolution with distance from the center of the defect in the (111) plane — along green and red lines shown in Figure 6(a) — is presented in Figure 6(b).

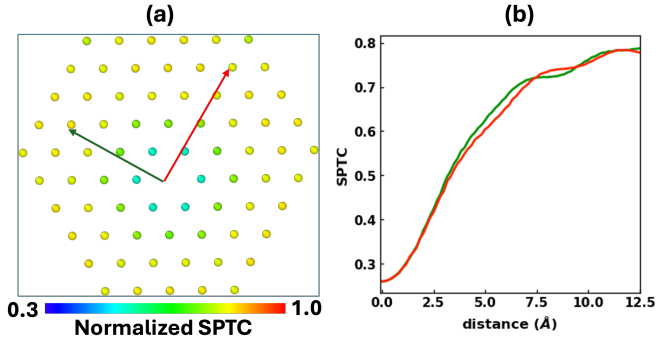


Figure 6: (a) Normalized SPTC data for a single-vacancy defect in crystalline Si, projected along the (111) plane intersecting the defect site. (b) The variation in SPTC with distance from the defect center along the red and green lines shown in panel (a).

Twin Grain Boundary in Silicon. In the SPTC analysis of the $\Sigma 3(112)/[1\bar{1}0]$ silicon grain boundary in Figure 7(a), the five-coordinated atoms (floating bonds) at the grain boundary exhibit lower SPTC compared to the bulk silicon and also influences the thermal activity of nearby atomic sites. Furthermore, a strong correlation between bonding environment and SPTC is evident: in Figure 7(b), the five-coordinated Si atoms labeled “i” show an SPTC reduction of around 79% compared to the bulk crystalline region labeled “ii.” Figure 7(c) further indicates that bond length distortions at the grain boundary contribute to the reduced SPTC, as atomic pairs with bond lengths exceed-

ing 2.36 Å (the bond length in diamond silicon) exhibit significantly lower SPTC values.

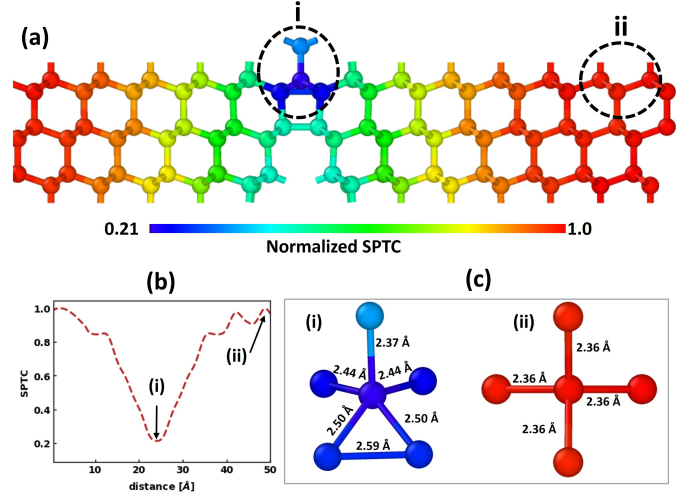


Figure 7: (a) SPTC for the Si $\Sigma 3(112)/[1\bar{1}0]$ twin grain boundary (GB), highlighting the correlation between SPTC values and bond lengths in different Si configurations: (i) five-fold coordination at the GB and (ii) four-fold coordination at the bulk region. The variation in SPTC for atoms along the line labelled “i” and “ii” is shown in (b), with their bond length distributions depicted in (c).

4.3. Mass and Chemical Disorder

The SPTC of the Ge-substituted $\text{Si}_{0.75}\text{Ge}_{0.25}$ crystal reveals a reduction in TC, consistent with expectations for a system exhibiting mass disorder. The average SPTC for Ge atoms in the $\text{Si}_{0.75}\text{Ge}_{0.25}$ crystal is approximately 7% lower than that for Si atoms. Notably, regions with a higher Si concentration display comparatively higher conductivity than those with greater Ge concentration. The TC values obtained for the $\text{Si}_{1-x}\text{Ge}_x$ system are as follows: for $x = 0.25$, the value is 1.50 W/mK; for $x = 0.5$, it remains 1.50 W/mK; and for $x = 0.75$, it increases to 2.46 W/mK. These results align with the trends observed in $\text{Si}_{1-x}\text{Ge}_x$ superlattices [31].

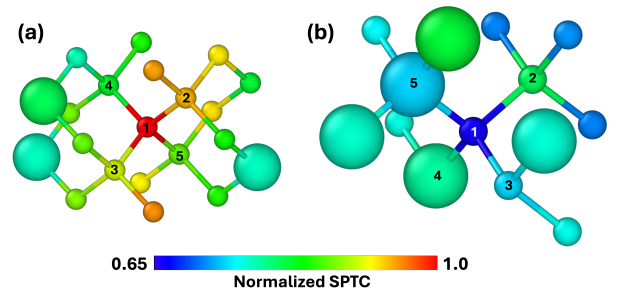


Figure 8: Bonding environment for Si atoms with (a) the highest and (b) the lowest SPTC in the $\text{Si}_{0.75}\text{Ge}_{0.25}$ crystal. In (a), the silicon atom (1) has the highest SPTC and is connected to silicon atoms (2, 3, 4, 5), which are also connected to other silicon atoms. In (b), the silicon atom (1), which has the lowest SPTC among silicon atoms in the system, is connected to two silicon atoms (2, 3) and two germanium atoms (4, 5).

Further, atomistic analysis of the $\text{Si}_{0.75}\text{Ge}_{0.25}$ crystal reveals distinct correlations between SPTC and local environment of

individual atoms. For example, a silicon atom exhibits the highest SPTC when connected to four neighboring silicons, which in turn are also connected with other silicon atoms. Conversely, a silicon atom exhibits the lowest SPTC when bonded to the germanium atoms and/or connected to silicon atoms which are connected to germanium atoms. Figure 8, provides a visual description of thermal characteristics of silicon atoms in different bonding environments within the Si-Ge system.

5. Conclusion

This study introduces the Space-Projected Thermal Conductivity (SPTC) methodology that employs Green-Kubo theory to map TC onto atomic sites, thus identifying more or less thermally active regions. To illustrate the utility of this approach, we calculated the SPTC to carbon, silicon, and silicon-germanium systems, showing that point, planar (grain boundary) and mass defects in these systems considerably reduce local TC. Although the developed methodology does not account for electronic contributions, limiting quantitative comparisons with experimental data, it effectively predicts thermal conduction paths consistent with known defect behavior in these materials.

Funding

This project was supported by ONR Grant N00014-23-1-2773. This work also used computational resources from the Advanced Cyberinfrastructure Coordination Ecosystem: Services & Support (ACCESS) program, through allocation DMR190002, MAT240030, funded by the U.S. National Science Foundation (NSF) grant number: 2138259, 2138286, 2138307, 2137603, and 2138296.

References

- [1] A. Minnich, Advances in the measurement and computation of thermal phonon transport properties, *Journal of Physics: Condensed Matter* 27 (5) (2015) 053202. doi:10.1088/0953-8984/27/5/053202.
- [2] X. Qian, R. Yang, Machine learning for predicting thermal transport properties of solids, *Materials Science and Engineering: R: Reports* 146 (2021) 100642. doi:10.1016/j.mser.2021.100642.
- [3] Y. Zeng, J. Dong, Fokker-planck equation for lattice vibration: Stochastic dynamics and thermal conductivity, *Phys. Rev. B* 99 (2019) 014306. doi:10.1103/PhysRevB.99.014306.
- [4] J. Dong, O. F. Sankey, C. W. Myles, Theoretical study of the lattice thermal conductivity in ge framework semiconductors, *Phys. Rev. Lett.* 86 (2001) 2361–2364. doi:10.1103/PhysRevLett.86.2361.
- [5] K. N. Subedi, K. Prasai, D. A. Drabold, Space-projected conductivity and spectral properties of the conduction matrix, *physica status solidi (b)* 258 (9) (Dec. 2020). doi:10.1002/pssb.202000438.
- [6] K. Prasai, K. N. Subedi, K. Ferris, P. Biswas, D. A. Drabold, Spatial projection of electronic conductivity: The example of conducting bridge memory materials, *physica status solidi (RRL) – Rapid Research Letters* 12 (9) (Jul. 2018). doi:10.1002/pssr.201800238.
- [7] K. N. Subedi, K. Kappagantula, F. Kraft, A. Nittala, D. A. Drabold, Electrical conduction processes in aluminum: Defects and phonons, *Physical Review B* 105 (10) (Mar. 2022). doi:10.1103/physrevb.105.104114.
- [8] K. N. Subedi, K. Nepal, C. Ugwumadu, K. Kappagantula, D. A. Drabold, Electronic transport in copper–graphene composites, *Applied Physics Letters* 122 (3) (Jan. 2023). doi:10.1063/5.0137086.
- [9] K. Nepal, C. Ugwumadu, A. Gautam, K. Kappagantula, D. A. Drabold, Electronic conductivity in metal–graphene composites: the role of disordered carbon structures, defects, and impurities, *Journal of Physics: Materials* 7 (2) (2024) 025003. doi:10.1088/2515-7639/ad261a.
- [10] K. Nepal, C. Ugwumadu, K. N. Subedi, K. Kappagantula, D. A. Drabold, Physical origin of enhanced electrical conduction in aluminum–graphene composites, *Applied Physics Letters* 124 (9) (Feb. 2024). doi:10.1063/5.0195967.
- [11] C. Ugwumadu, K. Subedi, R. Thapa, P. Apsangi, S. Swain, M. Kozicki, D. Drabold, Structure, vibrations and electronic transport in silicon sub-oxides: Application to physical unclonable functions, *Journal of Non-Crystalline Solids: X* 18 (2023) 100179. doi:https://doi.org/10.1016/j.nocx.2023.100179.
- [12] P. B. Allen, J. L. Feldman, Thermal conductivity of disordered harmonic solids, *Physical Review B* 48 (17) (1993) 12581–12588. doi:10.1103/physrevb.48.12581.
- [13] R. Kubo, M. Yokota, S. Nakajima, Statistical-mechanical theory of irreversible processes. ii. response to thermal disturbance, *Journal of the Physical Society of Japan* 12 (11) (1957) 1203–1211. doi:10.1143/jpsj.12.1203.
- [14] A. P. Thompson, H. M. Aktulga, R. Berger, D. S. Bolintineanu, W. M. Brown, P. S. Crozier, P. J. in 't Veld, A. Kohlmeyer, S. G. Moore, T. D. Nguyen, R. Shan, M. J. Stevens, J. Tranchida, C. Trott, S. J. Plimpton, LAMMPS - a flexible simulation tool for particle-based materials modeling at the atomic, meso, and continuum scales, *Computer Physics Communications* 271 (2022) 108171. doi:https://doi.org/10.1016/j.cpc.2021.108171.
- [15] P. Rowe, V. L. Deringer, P. Gasparotto, G. Csányi, A. Michaelides, An accurate and transferable machine learning potential for carbon, *The Journal of Chemical Physics* 153 (3) (Jul. 2020). doi:10.1063/5.0005084.
- [16] D. Unruh, R. V. Meidanshahi, S. M. Goodnick, G. Csányi, G. T. Zimányi, Gaussian approximation potential for amorphous si : H, *Physical Review Materials* 6 (6) (Jun. 2022). doi:10.1103/physrevmaterials.6.065603.
- [17] J. Tersoff, Modeling solid-state chemistry: Interatomic potentials for multicomponent systems, *Physical Review B* 39 (8) (1989) 5566–5568. doi:10.1103/physrevb.39.5566.
- [18] A. Stone, D. Wales, Theoretical studies of icosahedral c60 and some related species, *Chemical Physics Letters* 128 (5–6) (1986) 501–503. doi:10.1016/0009-2614(86)80661-3.
- [19] R. Thapa, C. Ugwumadu, K. Nepal, J. Tremblay, D. A. Drabold, Ab initio simulation of amorphous graphite, *Phys. Rev. Lett.* 128 (2022) 236402. doi:10.1103/PhysRevLett.128.236402.
- [20] C. Ugwumadu, R. Thapa, K. Nepal, D. A. Drabold, Atomistic nature of amorphous graphite, *European Journal of Glass Science and Technology Part B* 64 (2023) 16–22. doi:10.13036/17533562.64.1.18.
- [21] S. Nosé, A molecular dynamics method for simulations in the canonical ensemble, *Molecular Physics* 52 (2) (1984) 255–268. doi:10.1080/00268978400101201.
- [22] W. G. Hoover, Canonical dynamics: Equilibrium phase-space distributions, *Phys. Rev. A* 31 (1985) 1695–1697. doi:10.1103/PhysRevA.31.1695.
- [23] W. Shinoda, M. Shiga, M. Mikami, Rapid estimation of elastic constants by molecular dynamics simulation under constant stress, *Physical Review B* 69 (13) (2004) 134103.
- [24] V. Kapko, D. A. Drabold, M. F. Thorpe, Electronic structure of a realistic model of amorphous graphene, *physica status solidi (b)* 247 (5) (2010) 1197–1200. doi:10.1002/pssb.200945581.
- [25] Y. Li, F. Inam, A. Kumar, M. F. Thorpe, D. A. Drabold, Pentagonal puckering in a sheet of amorphous graphene, *physica status solidi (b)* 248 (9) (2011) 2082–2086. doi:10.1002/pssb.201147195.
- [26] A. Jain, S. P. Ong, G. Hautier, W. Chen, W. D. Richards, S. Dacek, S. Cholia, D. Gunter, D. Skinner, G. Ceder, K. A. Persson, Commentary: The materials project: A materials genome approach to accelerating materials innovation, *APL Materials* 1 (1) (Jul. 2013). doi:10.1063/1.4812323.
- [27] B. R. Djordjević, M. F. Thorpe, F. Wooten, Computer model of tetrahedral amorphous diamond, *Physical Review B* 52 (8) (1995) 5685–5689. doi:10.1103/physrevb.52.5685.
- [28] S. Fujii, A. Seko, Structure and lattice thermal conductivity of grain boundaries in silicon by using machine learning potential and molecular dynamics, *Computational Materials Science* 204 (2022) 111137.

[doi:10.1016/j.commatsci.2021.111137](https://doi.org/10.1016/j.commatsci.2021.111137).

- [29] C. Ugwumadu, R. Thapa, Y. Al-Majali, J. Trembly, D. A. Drabold, Formation of amorphous carbon multi-walled nanotubes from random initial configurations, *physica status solidi (b)* 260 (3) (2023) 2200527. [doi:https://doi.org/10.1002/pssb.202200527](https://doi.org/10.1002/pssb.202200527).
- [30] J. L. Feldman, M. D. Kluge, P. B. Allen, F. Wooten, Thermal conductivity and localization in glasses: Numerical study of a model of amorphous silicon, *Physical Review B* 48 (17) (1993) 12589–12602. [doi:10.1103/physrevb.48.12589](https://doi.org/10.1103/physrevb.48.12589).
- [31] Y. Lee, A. J. Pak, G. S. Hwang, What is the thermal conductivity limit of silicon germanium alloys?, *Physical Chemistry Chemical Physics* 18 (29) (2016) 19544–19548. [doi:10.1039/c6cp04388g](https://doi.org/10.1039/c6cp04388g).